



## Dual functional catalytic materials of Ni over Ce-modified CaO sorbents for integrated CO<sub>2</sub> capture and conversion

Hongman Sun<sup>a</sup>, Jianqiao Wang<sup>b</sup>, Jinhui Zhao<sup>c</sup>, Boxiong Shen<sup>b,\*,\*\*</sup>, Jeffrey Shi<sup>c</sup>, Jun Huang<sup>c,\*\*</sup>, Chunfei Wu<sup>a,b,d,\*</sup>



<sup>a</sup> School of Engineering and Computer Science, University of Hull, Hull, HU6 7RX, UK

<sup>b</sup> School of Energy and Environmental Engineering, Hebei University of Technology, Tianjin, 300401, China

<sup>c</sup> School of Chemical and Biomolecular Engineering, The University of Sydney, Sydney, NSW, 2037, Australia

<sup>d</sup> School of Chemistry and Chemical Engineering, Queen's University Belfast, Belfast, BT7 1NN, UK

### ARTICLE INFO

#### Keywords:

CO<sub>2</sub> capture and conversion  
Calcium looping  
The reverse water-gas shift  
Dual functional materials  
Ce-modified CaO sorbents

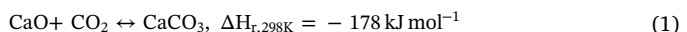
### ABSTRACT

Excessive anthropogenic CO<sub>2</sub> emission in the atmosphere is considered as one of the main contributions to the serious climate changes. However, with the growth of global economics, more fossil fuels will be consumed to feed the global activity, especially in developing countries. Thus, CO<sub>2</sub> needs to be captured for storage or converted to fuels or value-added chemicals. Herein, we propose and demonstrate a one-pot method synthesized dual functional materials (DFMs), which contain a sorbent coupled with a catalyst component, allowing the sorbent regeneration and CO<sub>2</sub> conversion to CO are performed simultaneously in a single reactor. This process requires no additional thermal energy for the regeneration of sorbents. In addition, CeO<sub>2</sub> is incorporated into the DFMs to largely enhance the stability of the materials for the process, and the influence of different Ce loadings on the performance of integrated CO<sub>2</sub> capture and conversion is studied. It is found that the DFMs with a Ca/Ni/Ce molar ratio of 1:0.1:0.033 displays almost 100% CO selectivity and 51.8% CO<sub>2</sub> conversion in the reverse water-gas shift (RWGS) reaction and a remarkable cyclic stability after 20 cycles of integrated CO<sub>2</sub> capture and conversion. Therefore, the incorporation of Ce into DFMs has two profits, for one thing, the oxygen vacancies generated by CeO<sub>2</sub> directly reduces the dissociated CO<sub>2</sub> regenerated from the DFMs, demonstrating the high CO yield; for another, the well-dispersed CeO<sub>2</sub>, which could act as a physical barrier, effectively prevents the growth and agglomeration of CaO crystallite and NiO species.

### 1. Introduction

Excessive anthropogenic CO<sub>2</sub> emission in the atmosphere is considered as one of the main contributions to the serious climate changes [1,2]. The 21st conference on global warming (COP21) reached a landmark agreement (the Paris Agreement) to limit the increase of the global average temperature to 2.0 °C in 2100 [3]. To achieve such an objective made on the Paris Agreement, CO<sub>2</sub> emissions from energy- and industry-related sources must decrease dramatically after 2030 and reach net-zero levels between 2060 and 2080 [4]. There are a number of materials (e.g., amine-based solvents [5,6], alkaline metal oxide-based sorbents [7,8], ionic liquids [9,10] and porous materials [11]) applicable for CO<sub>2</sub> capture from the use of fossil fuels. The carbon capture process usually relies on a temperature swing process for carbon capture and sorbent regeneration [12]. This process is energy

intensive. Thus, considerable efforts have been devoted to developing more efficient and economical CO<sub>2</sub> capture technologies. Calcium-Looping (CaL) process based on the reversible carbonation/calcination reaction of CaO (Eq. (1)) has been applied for large-scale CO<sub>2</sub> capture from fossil fuel power plants [13–15] as originally proposed by Shimizu et al. [16] because of the high reactivity with CO<sub>2</sub> (theoretical capture capacity of CaO is 17.8 mmol g<sup>-1</sup>) and the availability of low-cost natural CaO precursors [17–19]. The techno-economic modelling of CaL process has estimated that the carbon capture cost was \$ 16–44 per ton CO<sub>2</sub>, which is very competitive with the current amine scrubbing technologies costing about \$ 32–80 per ton CO<sub>2</sub> [20,21]. In addition, many efforts have been devoted to investigate the carbon capture performance of CaL process in realistic condition including the influences of CO<sub>2</sub> partial pressure, steam, SO<sub>2</sub> and O<sub>2</sub>, etc [22–24].



\* Corresponding author at: School of Engineering and Computer Science, University of Hull, Hull, HU6 7RX, UK.

\*\* Corresponding authors.

E-mail addresses: [shenbx@hebut.edu.cn](mailto:shenbx@hebut.edu.cn) (B. Shen), [jun.huang@sydney.edu.au](mailto:jun.huang@sydney.edu.au) (J. Huang), [c.wu@hull.ac.uk](mailto:c.wu@hull.ac.uk), [c.wu@qub.ac.uk](mailto:c.wu@qub.ac.uk) (C. Wu).

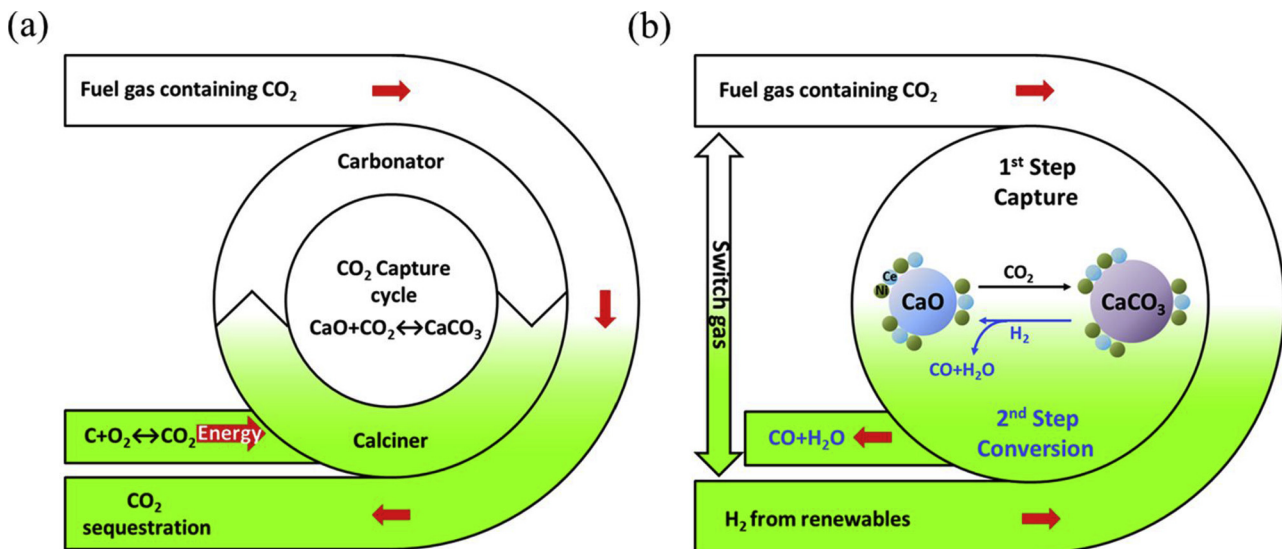


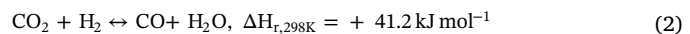
Fig. 1. Schematic diagram of (a) the conventional CaL process and (b) proposed process that integrates the RWGS process directly into the CO<sub>2</sub> capture process yielding a synthesis gas.

Currently, the great challenge of CaL process lies in the logistics and energy penalties of managing the concentrated CO<sub>2</sub>, which must be transported to an underground injection facility (CCS) or a processing plant for conversion to useful products (CCU) [25,26]. Compared to CCS, which is very expensive to run and could cause negative environmental impacts [27], CCU seems to be more attractive and promising due to CO<sub>2</sub> can be used as carbon source to offer an alternative to produce carbon-containing value-added products [28]. Thus, there is a growing interest in exploring the possibility of utilizing the captured CO<sub>2</sub> as a carbon feedstock and converting it to fuels or value-added chemicals [29–31].

Robert J. Farrauto's research group [25,29] reported that using dual function materials (DFMs) for CO<sub>2</sub> capture and the conversion to synthetic natural gas at the same temperature (320 °C) simultaneously in the same reactor, requiring no additional heat input. The DFMs consisted of Ru as the methanation catalyst and nano-dispersed CaO as the CO<sub>2</sub> adsorbent. Both active sites were supported on a porous γ-Al<sub>2</sub>O<sub>3</sub> carrier. A spillover process drove CO<sub>2</sub> from the sorbent to the Ru sites where methanation occurred using stored H<sub>2</sub> from excess renewable power. However, in this process, the low loading of CaO (10 wt.%) resulted in a relatively low CO<sub>2</sub> capture capacity and consequent low methane yield. In addition, the main drawback of the mentioned process is the substantial utilization of noble metal Ru (10 wt.%), which can greatly increase the industrialization cost of such materials. In addition, Christoph Müller's research group [31] proposed and experimentally demonstrated a process that directly integrated CO<sub>2</sub> utilization (dry reforming of methane) into CO<sub>2</sub> capture allowing for the full conversion of the CO<sub>2</sub> captured. Importantly, a non-precious metal catalyst (Ni/MgO-Al<sub>2</sub>O<sub>3</sub>) and an inexpensive naturally occurring CO<sub>2</sub> sorbent (limestone) were utilized in this integrated process. This process is attractive economically and the coupled reactions are performed in a single reactor to avoid the transportation of solid sorbent which requires a strong mechanical strength of the sorbent in conventional CaL. However, the synthesis of materials consists of two discrete steps including the synthesis of dry reforming catalyst and the mixture of the catalyst with CO<sub>2</sub> capture sorbents, which is complex.

Another important product from the reduction of CO<sub>2</sub> is CO, which serves as a feedstock for producing chemicals and fuels via Fischer-Tropsch synthesis [32,33]. The reverse water-gas shift (RWGS, Eq. (2)) is one of the most established reactions to convert CO<sub>2</sub> into the water and CO [34,35], which can be exploited for introducing carbonyl functionalities into a plethora of molecules in both an academic and an

industrial setting [36,37].



However, the major challenge for the CaO-based sorbents and the Ni-based catalysts is the fast decay of CO<sub>2</sub> capture performance and the deactivation of catalytic performance with the number of cycles, respectively [38]. CeO<sub>2</sub>, with a Tamman temperature of 1064 °C [39,40], also has a possibility to be incorporated into CaO as a good inert material. Wang et al. synthesized a series of Ce-doped sorbents by a simple sol-gel method, and the sample (Ca/Ce = 15:1) showed a favourable capture capacity and cyclic stability, maintaining a CO<sub>2</sub> uptake capacity of 13.4 mmol g<sup>-1</sup> after 18 cycles [39]. In addition, ceria exhibits excellent redox properties due to the rapid reduction of Ce<sup>4+</sup> to Ce<sup>3+</sup> associated with the creation of oxygen vacancies [41]. It has the ability to release oxygen under reducing atmosphere and storing oxygen under an oxidizing environment by filling oxygen vacancies [42]. The introduction of CeO<sub>2</sub> acting as a support to improve the catalytic activity has been studied extensively for the development of Ni-based catalysts [43–45]. Du et al. studied the catalytic properties of Ni/CeO<sub>2</sub> nanostructure for CO<sub>2</sub> reforming of methane and found that the strong metal-support effect can be helpful to prevent the sintering of Ni particles, reducing the deactivation of catalytic activity [43]. In addition, a series of Ni/CeO<sub>2</sub> catalysts with Ni loading ranging from 7 to 26 wt% were prepared via combustion synthesis and the stability was enhanced during methane dry reforming process [44]. Here, we propose and demonstrate a one-pot method to synthesize DFMs, which contain a sorbent CaO coupled with a catalyst component Ni, as well as a physical barrier Ce, allowing the sorbent regeneration and CO<sub>2</sub> conversion to perform simultaneously in a single reactor via the reaction in Eq. (3).



The comparison between the conventional CaL process and the proposed process that integrates RWGS directly into CO<sub>2</sub> capture yielding a synthesis gas is shown in Fig. 1. Obviously, in the conventional CaL process as shown in Fig. 1a, two reactors including a carbonator and a calciner as well as the energy produced by the combustion are required for the cyclic performance of sorbents [46]. However, in this integrated process (Fig. 1b), both CO<sub>2</sub> capture and conversion are performed at the same temperature and a single reactor without an energy-intensive thermal swing process, eliminating the energy requirement, corrosion, and transportation issues associated

with CCS. To the best of our knowledge, the simultaneous conversion of the captured  $\text{CO}_2$  in a single reactor via the one-pot synthesized DFM in the RWGS process has not been reported yet. In addition, the influence of different Ce loadings, as well as the mechanism on the performance of integrated  $\text{CO}_2$  capture and conversion, were studied in details.

## 2. Experimental section

### 2.1. Dual functional materials preparation

All the DFM were synthesized by a standard sol-gel combustion method reported by Santos et al. [47] and a typical synthesis process is as follows. Initially, predetermined amounts of analytical reagent-grade calcium nitrate tetrahydrate ( $\text{Ca}(\text{NO}_3)_2 \cdot 4\text{H}_2\text{O}$ , Sigma-Aldrich, 99.99%), nickel nitrate hexahydrate ( $\text{Ni}(\text{NO}_3)_2 \cdot 6\text{H}_2\text{O}$ , Sigma-Aldrich, 99.99%) and citric acid monohydrate (Sigma-Aldrich, 99.99%) working as the chelation agent were added to distilled water at room temperature (water, citric acid and  $\text{Ni}^{2+}$  to  $\text{Ca}^{2+}$  molar ratios were 40:1, 1:1 and 0.1:1, respectively). Subsequently, for the Ce-doped DFM, appropriate amounts of cerium nitrate hexahydrate ( $\text{Ce}(\text{NO}_3)_2 \cdot 6\text{H}_2\text{O}$ , Sigma-Aldrich, 99.99%) were added to the mixture solution and the  $\text{Ce}^{2+}$  to  $\text{Ca}^{2+}$  molar ratios were 1:60 and 1:30. Then, the mixture was continuously stirred at 80 °C to form a well-dispersed translucent pale green sol. The pale green sol was dried overnight at 130 °C. After drying, a low-density foam was obtained. The foam was easily crushed in a porcelain mortar and then calcined in a muffle furnace at 850 °C for 5 h with a heating rate of 2 °C min<sup>-1</sup>. The obtained samples are designated as  $\text{Ca}_1\text{Ni}_{0.1}$ ,  $\text{Ca}_1\text{Ni}_{0.1}\text{Ce}_{0.017}$ , and  $\text{Ca}_1\text{Ni}_{0.1}\text{Ce}_{0.033}$ , respectively. Pure sol-gel CaO was also prepared according to the same method used as the reference adsorbent.

### 2.2. Dual functional materials characterization

Elemental analyses of the catalysts were performed with a Perkin Elmer Optima 5300DV inductively coupled plasma optical emission spectrometer (ICP-OES) equipped with a Teflon sample introduction system. The sample was dissolved into the nitric acid and heated in the CEM MARS microwave system to 180 °C for 10 min and then cooled down to room temperature.

Powder X-ray diffraction (XRD) was performed on PANalytical empyrean series 2 diffractometer with  $\text{Cu K}\alpha$  radiation. The data was collected in the 5–80° 2 $\theta$  range and analysed by Xpert Highscore plus software. Scherrer equation was used to estimate the average crystallite size based on the diffraction peaks at 42.2° of NiO particles and 28.5° of  $\text{CeO}_2$  particles.

Nitrogen adsorption-desorption isotherms were measured using ASAP 2020 analyzer at 77 K. Brunauer-Emmett-Teller (BET) surface area was measured using the adsorption branch data in the relative pressure ( $P/P_0$ ) range from 0.06 to 0.2, and the micropore volume ( $V_{\text{micro}}$ ) was calculated by the t-plot method. The pore size distribution was calculated by the Barrett-Joyner-Halenda (BJH) method using nitrogen desorption branch data.

The surface morphology of samples was measured by a Stereoscan 360 Scanning electron microscopy (SEM) coupled with an energy dispersive X-ray spectrometer (EDX). The detailed structure of DFM was characterized by transmission electron microscopy (TEM, a JEOL 2010) with an elemental mapping and high-resolution transmission electron microscopy (HRTEM, FEI talos F200). The preparation of samples for analysis involved being ultrasonically dispersed in absolute acetone and dropped cast on carbon-coated Cu grids.

The atomic concentrations of metals at the surface of the DFM were determined by X-ray photoelectron spectrometer (XPS, Thermo Fisher Scientific Escalab 250Xi) using  $\text{Mg K}\alpha$  radiation. The binding energies were calibrated using the C1s peak (284.6 eV) of adventitious carbon. The ratios of  $\text{Ce}^{3+}$  to  $\text{Ce}^{4+}$  and  $\text{Ni}^{2+}$  to  $\text{Ni}^{3+}$  in DFM were calculated

using the deconvoluted Ce3d and Ni2p peak areas of the XPS spectra, respectively.

Raman spectroscopy (Thermo Scientific) was used to characterize the coke deposition. The Raman spectra were acquired in the range of 500–3500 cm<sup>-1</sup> using a laser with a wavelength of 514.5 nm. The spectral resolution employed was 4 cm<sup>-1</sup>.

### 2.3. Integrated $\text{CO}_2$ capture and conversion

A fixed-bed reactor coupled with a gas analyser operated under atmospheric pressure (as shown in Fig. S1) was used to determine the integrated  $\text{CO}_2$  capture and conversion performance of the DFM. Two sets of experiment were conducted to determine the influence of process parameters: the effect of different DFM using  $\text{CaO}$ ,  $\text{Ca}_1\text{Ni}_{0.1}$ ,  $\text{Ca}_1\text{Ni}_{0.1}\text{Ce}_{0.017}$  and  $\text{Ca}_1\text{Ni}_{0.1}\text{Ce}_{0.033}$ ; the influence of carbonation and conversion temperatures of 650, 700, 750 °C. In a typical experiment, 250 mg powdered DFM was loaded into the tube fixed by the quartz wool. The sample received a pre-reduction at 650 °C in a flow of 5%  $\text{H}_2$  balanced with  $\text{N}_2$  for 3 h with the heating rate of 10 °C min<sup>-1</sup>. After reduction, the carbonation reaction was conducted in 15%  $\text{CO}_2$  balanced with  $\text{N}_2$  (100 mL min<sup>-1</sup>) for 25 min. Subsequently, the DFM were regenerated under 5%  $\text{H}_2$  in  $\text{N}_2$  (100 mL min<sup>-1</sup>) after the fixed reactor was purged by  $\text{N}_2$  for 5 min. With the further increase of temperature to 700 °C and then 750 °C, the carbonation reaction was carried out in 15%  $\text{CO}_2$  balanced with  $\text{N}_2$  (100 mL min<sup>-1</sup>) for 25 min. After the fixed reactor was purged by  $\text{N}_2$  for 5 min, the regeneration of DFM was performed under 5%  $\text{H}_2$  in  $\text{N}_2$  (100 mL min<sup>-1</sup>).

In-situ DRIFTS experiments were conducted by an FTIR spectrometer (JASCO-4600) coupled with a DRIFTS cell (Bruker). All spectra were recorded over accumulative 32 scans with a resolution of 4 cm<sup>-1</sup> in the range of 4000–400 cm<sup>-1</sup>. Prior to each experiment, the sample (~5 mg) was pre-reduced in 5%  $\text{H}_2$  stream balanced with  $\text{N}_2$  (100 mL min<sup>-1</sup>) at 650 °C for 30 min. And then the carbonation was performed in 15%  $\text{CO}_2$  balanced with  $\text{N}_2$  for 25 min. Subsequently, the DFM were regenerated under 5%  $\text{H}_2$  in  $\text{N}_2$  (100 mL min<sup>-1</sup>) after the in-situ reactor was purged by  $\text{N}_2$  for 5 min.

### 2.4. Cyclic $\text{CO}_2$ capture and conversion tests

Cyclic  $\text{CO}_2$  capture and conversion performance of DFM was conducted in a fixed-bed reactor coupled with a gas analyser under atmospheric pressure (as shown in Fig. S1). Approximately 250 mg of powdered DFM was loaded into the tube fixed by the quartz wool. The sample received a pre-reduction at 650 °C in a flow of 5%  $\text{H}_2$  balanced with  $\text{N}_2$  for 3 h with the heating rate of 10 °C min<sup>-1</sup>. Subsequently, the carbonation reaction was conducted in 15%  $\text{CO}_2$  balanced with  $\text{N}_2$  (100 mL min<sup>-1</sup>) for 25 min. After carbonation, the DFM was regenerated under 5%  $\text{H}_2$  in  $\text{N}_2$  (100 mL min<sup>-1</sup>) after the fixed reactor was purged by  $\text{N}_2$  for 3 min. In total, 20 cycles of the integrated  $\text{CO}_2$  capture and conversion process were performed.

## 3. Results and discussion

### 3.1. Characterization of fresh dual functional materials

ICP-OES is used to obtain elemental analysis data for DFM, and the results are shown in Table 1. The atomic ratio of Ni to Ca are around 0.1 for all the DFM, which is inconsistent with the predetermined metal contents. As for  $\text{Ca}_1\text{Ni}_{0.1}\text{Ce}_{0.017}$  and  $\text{Ca}_1\text{Ni}_{0.1}\text{Ce}_{0.033}$ , the atomic ratios of Ce to Ca are 0.017 and 0.032, respectively, which are used for the investigation of the influence of Ce loadings on integrated  $\text{CO}_2$  capture and conversion.

The XRD patterns of fresh DFM are presented in Fig. 2. The results evidence the presence of CaO in fresh samples, along with low-intensity peaks of  $\text{Ca}(\text{OH})_2$ . It is attributed to the reaction between CaO powder and moisture in the cooling process of calcination and storage. After the

**Table 1**

Elemental analysis, average crystallite size and textural properties and of fresh DFM s.

Samples	Molar ratio <sup>a</sup>			NiO <sup>b</sup>	CeO <sub>2</sub> <sup>b</sup>	S <sub>BET</sub> <sup>c</sup>	V <sub>p</sub> <sup>d</sup>
	Ca	Ni	Ce	(nm)	(nm)	(m <sup>2</sup> g <sup>-1</sup> )	(cm <sup>3</sup> g <sup>-1</sup> )
CaO	1	0	0	n.a.	n.a.	38.5	0.15
Ca <sub>1</sub> Ni <sub>0.1</sub>	1	0.10	0	15	n.a.	12.8	0.11
Ca <sub>1</sub> Ni <sub>0.1</sub> Ce <sub>0.017</sub>	1	0.09	0.017	12	8	22.5	0.20
Ca <sub>1</sub> Ni <sub>0.1</sub> Ce <sub>0.033</sub>	1	0.10	0.032	12	8	20.7	0.14

<sup>a</sup> Molar ratios normalized with Ca = 1 measured by ICP.

<sup>b</sup> Average crystallite size calculated by Scherrer equation.

<sup>c</sup> BET surface areas.

<sup>d</sup> Total pore volume measured at a relative pressure (P/P<sub>0</sub>) of 0.99.

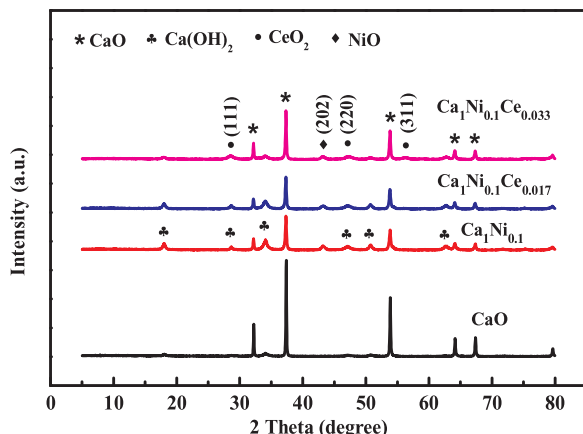


Fig. 2. XRD patterns of fresh DFM s.

incorporation of Ni, the DFM s exhibit a diffraction peak at  $2\theta = 43.2^\circ$ , indicating the characteristic peak of NiO (2 0 2) [48]. The average crystallite size corresponding to NiO phase is calculated as 15, 12, and 12 nm for Ca<sub>1</sub>Ni<sub>0.1</sub>, Ca<sub>1</sub>Ni<sub>0.1</sub>Ce<sub>0.017</sub>, and Ca<sub>1</sub>Ni<sub>0.1</sub>Ce<sub>0.033</sub>, respectively. Therefore, it is concluded that CeO<sub>2</sub>, considered as a physical barrier, prevented the growing and agglomeration of the NiO crystallite and led to the decrease of the average crystallite size of NiO, which has been reported in other literature [49]. According to the Scherrer equation, the sharp and broad diffraction peaks are related to the large and small average crystallite size, respectively [50]. So the broad diffraction peak at  $28.5^\circ$  in Ca<sub>1</sub>Ni<sub>0.1</sub>Ce<sub>0.033</sub> is corresponding to CeO<sub>2</sub> instead of Ca(OH)<sub>2</sub> due to the large crystallite size property of Ca(OH)<sub>2</sub>. In addition, the appearance of diffraction peaks at 47.3 and 56.3 ° pertaining to CeO<sub>2</sub>

crystallite phase is also obvious in the Ce-doped samples.

N<sub>2</sub> adsorption-desorption isotherms and pore size distributions are conducted to determine the structure of the DFM s (Fig. 3). Textural properties derived from different DFM s are summarised in Table 1. All the isotherms obtained for DFM s exhibit a type IV isotherm shape. The shape of the hysteresis loops for all DFM s is type H3 resulting from the slit-shaped pores generated by the addition of citric acid. The surface area ( $12.8 \text{ m}^2 \text{ g}^{-1}$ ) and pore volume ( $0.11 \text{ cm}^3 \text{ g}^{-1}$ ) of Ca<sub>1</sub>Ni<sub>0.1</sub> are lower than those of the reference sol-gel CaO ( $38.5 \text{ m}^2 \text{ g}^{-1}$  and  $0.15 \text{ cm}^3 \text{ g}^{-1}$ , respectively) due to the introduction of NiO particles. With the doping of Ce, the BET surface area and pore volume are slightly increased. The BJH pore size distribution (Fig. 3b) indicates the formation of pores smaller than 4 nm in Ca<sub>1</sub>Ni<sub>0.1</sub>Ce<sub>0.017</sub> and Ca<sub>1</sub>Ni<sub>0.1</sub>Ce<sub>0.033</sub> and the disappearance of the mesopores ranging from 4 nm to 10 nm.

The morphologies and active components of the fresh DFM s are determined by SEM-EDX analysis, as shown in Fig. 4. In the calcination process of DFM s preparation using the sol-gel method, a large amount of gas and heat would release during the reaction and enhance the formation of a porous and fluffy structure [51]. Therefore, it can be observed in Fig. 4a that the synthesized sol-gel CaO possesses a fluffy and porous structure, which is in agreement with the pore size distribution in Fig. 3b. After the introduction of NiO into the adsorbents, a peak belonging to Ni is observed in the EDX results and the surface of the DFM s become loose, which is favorable for the reaction between CaO and CO<sub>2</sub>. The morphologies of the CeO<sub>2</sub>-doped DFM s are much different from others, appearing as a more loose structure with lots of micropores and mesopores. This morphology can contribute to the excellent cyclic performance of CO<sub>2</sub> capture due to the efficient diffusion of CO<sub>2</sub> inward in the sorbent and reacts with CaO in the interior and exterior of the sorbent at the same time [52]. In the carbonation process, there exists a critical product layer thickness of CaCO<sub>3</sub>, at which the reaction transforms from the kinetic-controlled stage of carbon capture to the diffusion-controlled stage [53]. When the product layer thickness achieves this critical value, there is more CaO reacting with CO<sub>2</sub> for the Ce-doped DFM s. In addition, the EDX results show a small peak assigned to Ce in Fig. 4c and d indicating the successful incorporation of Ce into DFM s. It is noted that doping cerium can bring a large number of oxygen vacancies and an improved oxygen transport capacity ( $\text{Ce}^{3+} \leftrightarrow \text{Ce}^{4+}$ ) [54,55]. The oxygen vacancy is favorable to the diffusion of CO<sub>2</sub> and the mobility of O<sup>2-</sup> according to the proposed adsorption mechanism of CO<sub>2</sub> [56]. The process is shown as follows:

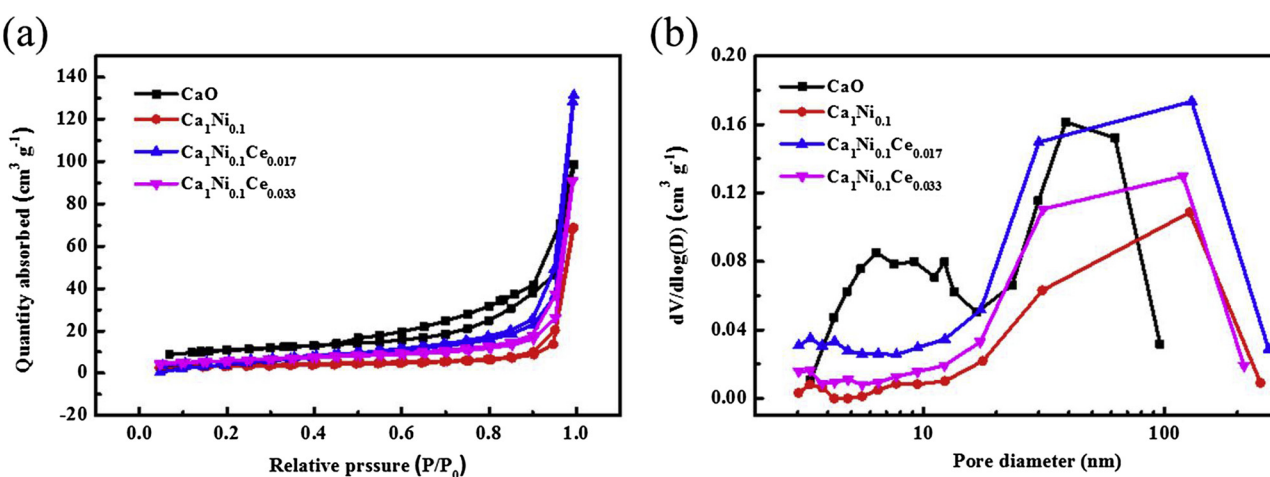


Fig. 3. (a) N<sub>2</sub> adsorption-desorption isotherms and (b) pore size distribution calculated from the BJH desorption branch.

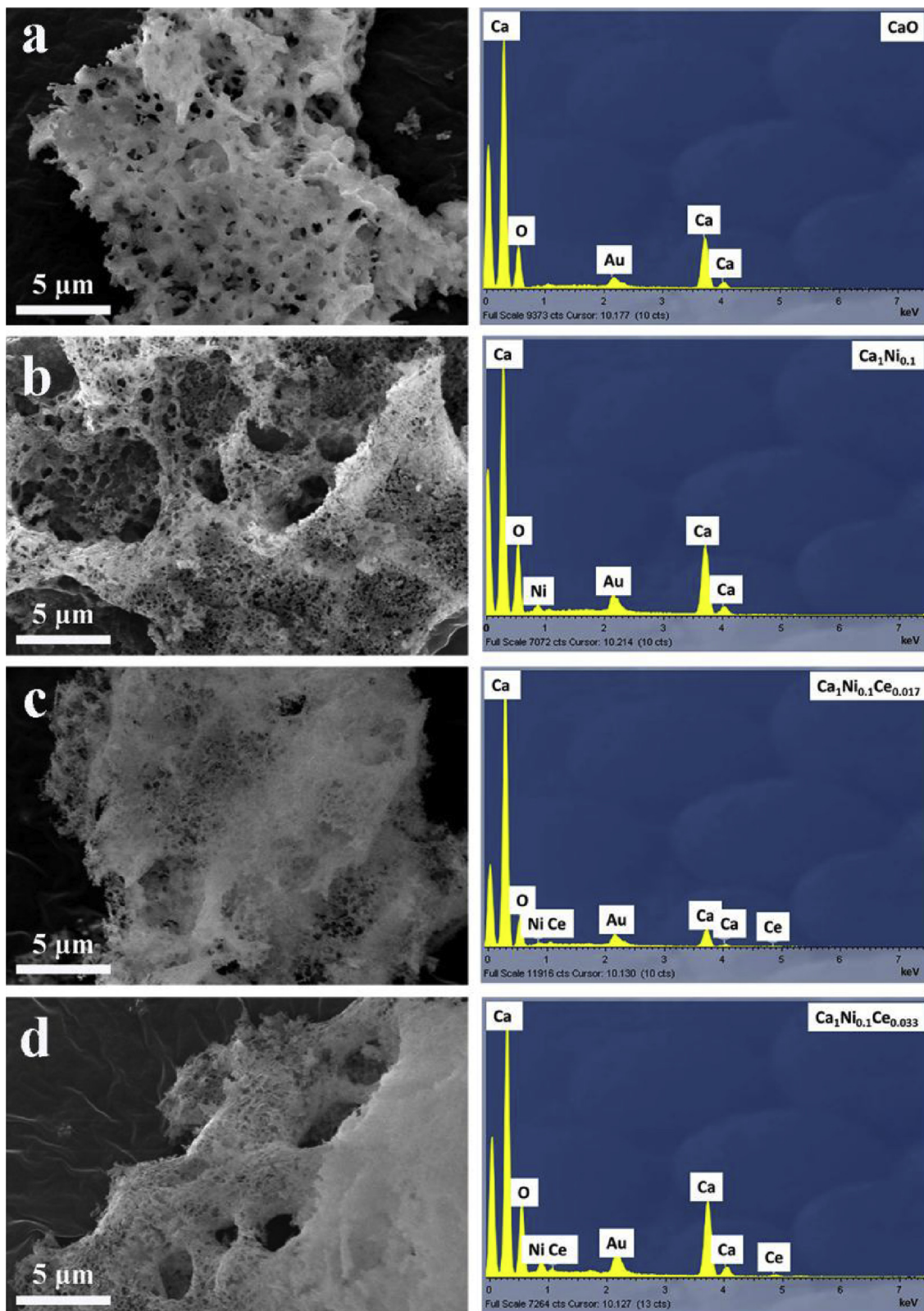
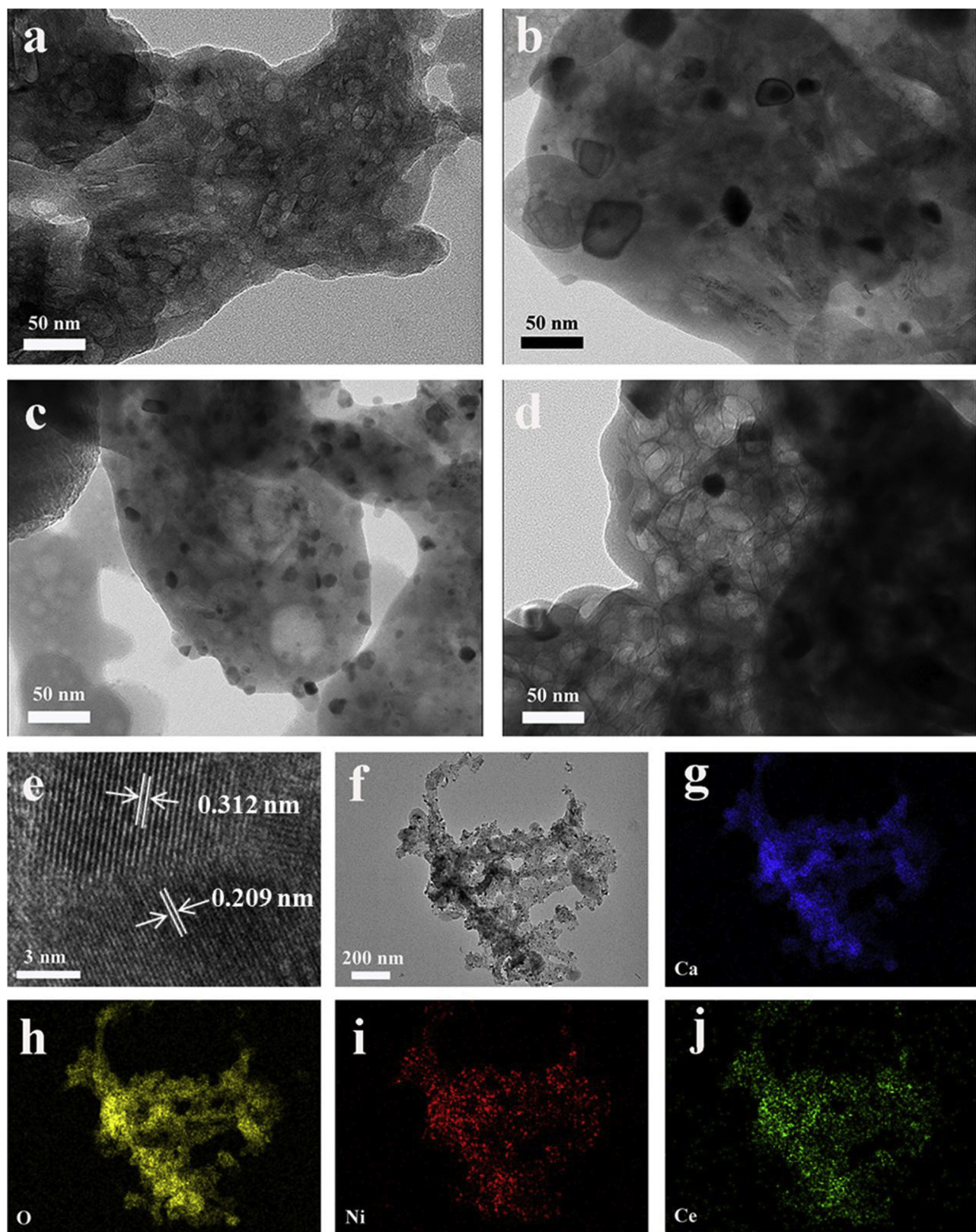


Fig. 4. SEM images and EDX of fresh DFM (a) CaO, (b) Ca<sub>1</sub>Ni<sub>0.1</sub>, (c) Ca<sub>1</sub>Ni<sub>0.1</sub>Ce<sub>0.017</sub>, (d) Ca<sub>1</sub>Ni<sub>0.1</sub>Ce<sub>0.033</sub>.



The porous structure and particle distribution are shown in Fig. 5. The pure sol-gel CaO as shown in Fig. 5a exhibits a porous structure without apparent particles, which is in agreement with the SEM results. There are irregular particles distributed on the sol-gel CaO matrix,

which are assigned to NiO particles as shown in Fig. 5. As for the Ce-doped DFM, the metal particle size exhibits a dramatic decrease. It is verified that nano-sized particles with the more coordinative unsaturated sites on the surfaces are easier to absorb CO<sub>2</sub>, and they enable faster diffusion rate of CO<sub>2</sub> through the layer of formed CaCO<sub>3</sub> [57,58].



**Fig. 5.** TEM images of fresh DFM<sub>s</sub> (a) CaO, (b) Ca<sub>1</sub>Ni<sub>0.1</sub>, (c) Ca<sub>1</sub>Ni<sub>0.1</sub>Ce<sub>0.017</sub>, (d) Ca<sub>1</sub>Ni<sub>0.1</sub>Ce<sub>0.033</sub>. High-resolution TEM (e) and elemental mappings (f–i) of Ca<sub>1</sub>Ni<sub>0.1</sub>Ce<sub>0.033</sub>.

With further increase of Ce loading, the Ca<sub>1</sub>Ni<sub>0.1</sub>Ce<sub>0.033</sub> displays the obvious lattice fringes (Fig. 5e) indicating the high crystallinity of CeO<sub>2</sub> and NiO. The interplanar spacing of 0.312 nm and 0.209 nm represent (111) lattice plane of CeO<sub>2</sub> and (202) lattice plane of NiO, respectively.

The elemental mapping of Ca<sub>1</sub>Ni<sub>0.1</sub>Ce<sub>0.033</sub> demonstrates the uniform distribution of Ca, O, Ni and Ce elements, which is effective to delay the sintering and prevent the aggregation of CaO particles, resulting in an outstanding stability.

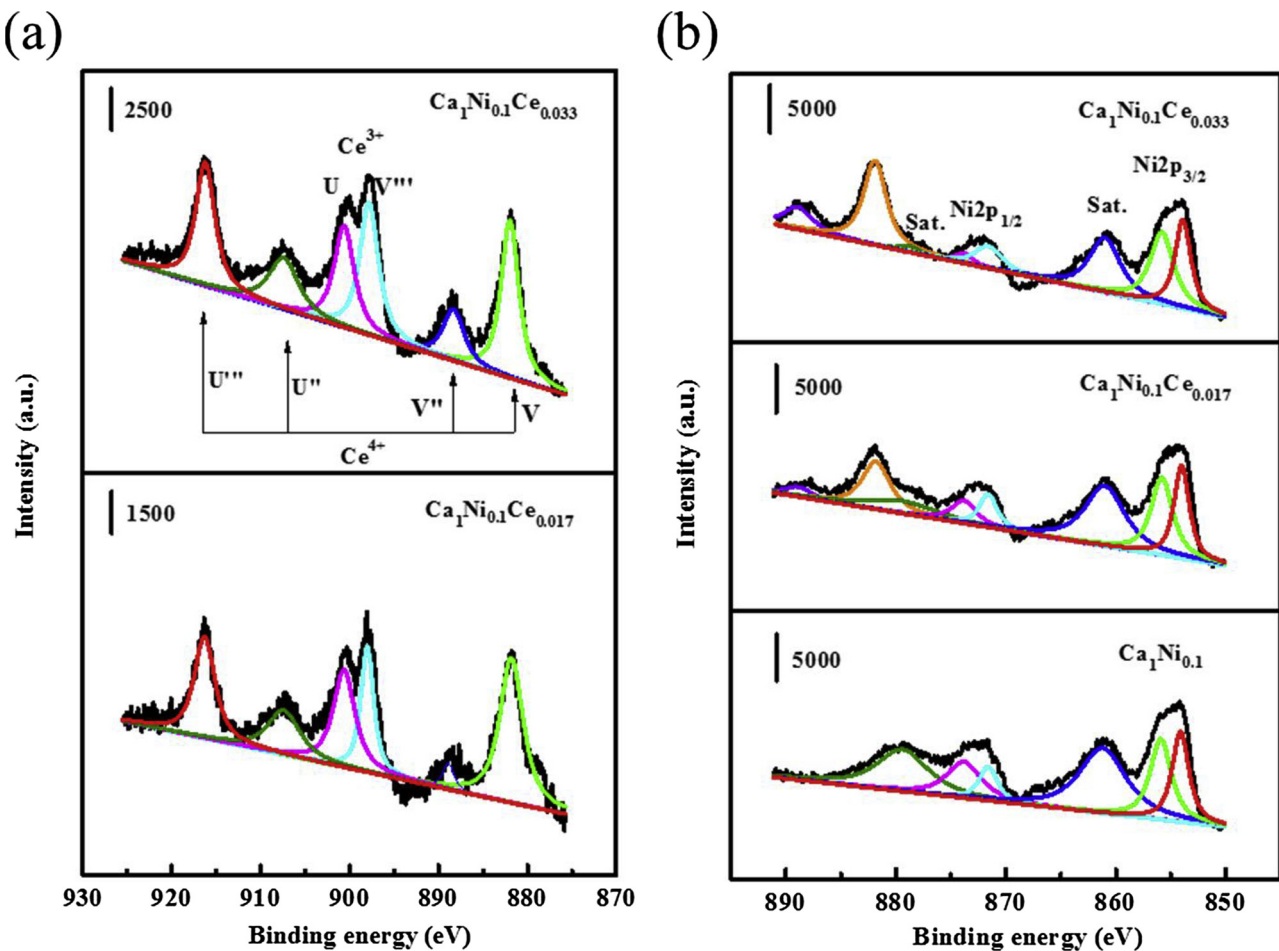
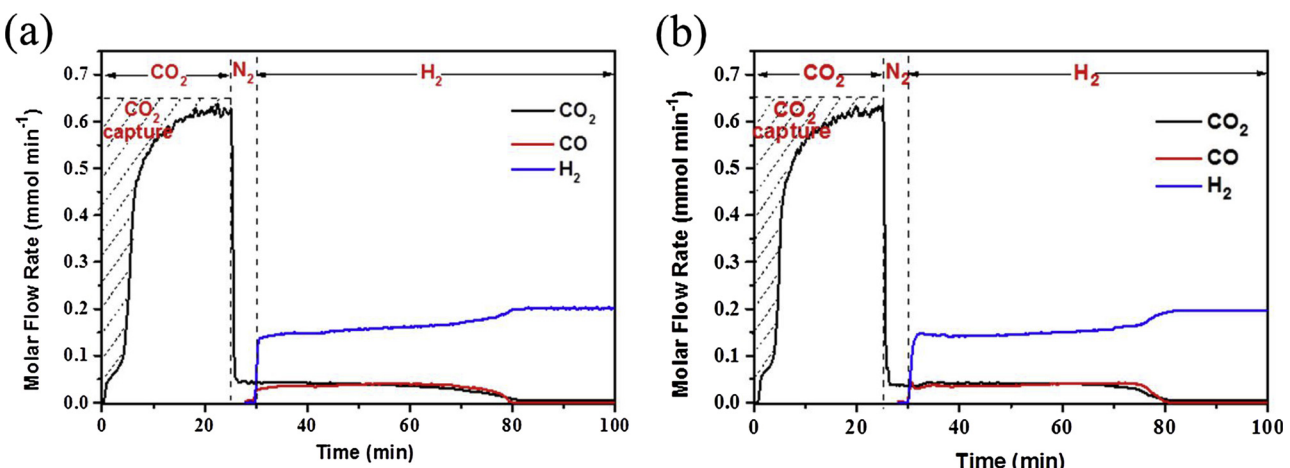


Fig. 6. XPS spectra of (a) Ce3d and (b) Ni2p of fresh DFMs.

**Table 2**  
XPS results of DFMs.

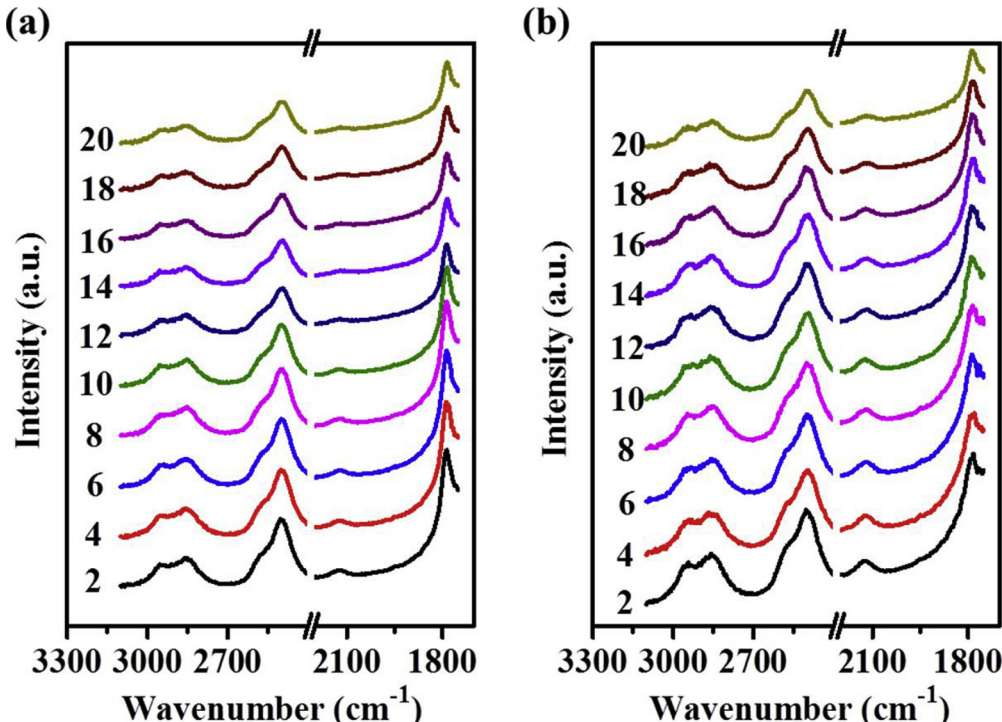
Samples	Ce <sup>3+</sup> /Ce <sup>4+</sup>	Ni <sup>2+</sup> /Ni <sup>3+</sup>
CaO	/	/
Ca <sub>1</sub> Ni <sub>0.1</sub>	/	0.72
Ca <sub>1</sub> Ni <sub>0.1</sub> Ce <sub>0.017</sub>	0.52	0.90
Ca <sub>1</sub> Ni <sub>0.1</sub> Ce <sub>0.033</sub>	0.58	1.10

XPS analysis is performed on DFMs to identify the valence states and the chemical composition. The Ce3d spectra are complicated due to the existence of two different cerium oxidation states, the hybridization of the O2p valence band with the Ce4f level as well as spin-orbit coupling [56]. The main features of the Ce3d are composed of ten peaks marked as u and v, which are corresponding to five pairs of spin-orbit components attributed to 3d<sub>3/2</sub> and 3d<sub>5/2</sub> [59,60]. Six of the peaks labelled as U, U'', U''', V, V'', V''' are associated to Ce<sup>4+</sup> ions, and the other four peaks denoted by U°, U', V°, V' are connected to Ce<sup>3+</sup> ions. As shown in Fig. 6a, six main binding energy peaks can be observed including 916.3,

Fig. 7. Integrated CO<sub>2</sub> capture and conversion reactions at 650 °C of (a) Ca<sub>1</sub>Ni<sub>0.1</sub>; (b) Ca<sub>1</sub>Ni<sub>0.1</sub>Ce<sub>0.033</sub>.

**Table 3**The integrated  $\text{CO}_2$  capture and conversion performance, as well as turnover frequency (TOF) of different DFMs at 650 °C.

Samples	Capture capacity <sup>a</sup> mmol g <sup>-1</sup>	$\text{CO}_2$ yield <sup>a</sup> mmol g <sup>-1</sup>	CO yield <sup>a</sup> mmol g <sup>-1</sup>	Carbon Balance (%)	$\text{CO}_2$ conversion (%)	TOF <sup>b</sup> s <sup>-1</sup>
CaO	15.7	7.6	3.2	68.4	23.4	/
Ca <sub>1</sub> Ni <sub>0.1</sub>	15.0	7.2	6.9	94.4	46.0	0.72
Ca <sub>1</sub> Ni <sub>0.1</sub> Ce <sub>0.017</sub>	14.2	6.8	7.2	98.0	50.7	0.75
Ca <sub>1</sub> Ni <sub>0.1</sub> Ce <sub>0.033</sub>	14.1	6.7	7.3	99.2	51.8	0.78

<sup>a</sup> Calculated by per gram of sorbents.**Fig. 8.** In-situ DRIFTS spectra of the species formed over (a) Ca<sub>1</sub>Ni<sub>0.1</sub>; (b) Ca<sub>1</sub>Ni<sub>0.1</sub>Ce<sub>0.033</sub> after switching gas to H<sub>2</sub> for 2, 4, 6, 8, 10, 12, 14, 16, 18 and 20 min.

907.4, 888.9 and 881.8 eV assigned to Ce<sup>4+</sup> 3d<sub>5/2</sub>, as well as 900.6 and 898.0 eV ascribed to Ce<sup>3+</sup> 3d<sub>3/2</sub>. Therefore, Ce mainly exists in +3 and +4 oxidation states in the DFMs. The Ce<sup>3+</sup> to Ce<sup>4+</sup> ratios of the Ca<sub>1</sub>Ni<sub>0.1</sub>Ce<sub>0.017</sub> and the Ca<sub>1</sub>Ni<sub>0.1</sub>Ce<sub>0.033</sub> are 0.52 and 0.58 (Table 2), respectively, indicating more oxygen vacancies created by the Ce<sup>3+</sup> with the increase of Ce loading.

By using a Gaussian fitting method, the Ni2p spectrum (Fig. 6b) is fitted by considering two spin-orbit doublet characteristic of Ni<sup>2+</sup> and Ni<sup>3+</sup> and two shakeup satellites [61]. According to the fitting data, the fitting peaks at the binding energy of 854.1 and 871.6 eV are indexed to Ni<sup>2+</sup>, while the fitting peaks at the binding energy of 855.8 and 873.8 eV are ascribed to Ni<sup>3+</sup> [62]. In addition, the satellite peaks at 861.0 eV and 879.4 eV are two shake-up type peaks of Ni at the high binding energy side of the Ni2p<sub>3/2</sub> and Ni2p<sub>1/2</sub> edge, respectively [63]. Two peaks at 881.8 and 888.9 eV of both Ca<sub>1</sub>Ni<sub>0.1</sub>Ce<sub>0.017</sub> and Ca<sub>1</sub>Ni<sub>0.1</sub>Ce<sub>0.033</sub> are caused by the introduction of Ce. Compared to the Ca<sub>1</sub>Ni<sub>0.1</sub>, the Ni<sup>2+</sup> to Ni<sup>3+</sup> ratios of the Ca<sub>1</sub>Ni<sub>0.1</sub>Ce<sub>0.017</sub> and Ca<sub>1</sub>Ni<sub>0.1</sub>Ce<sub>0.033</sub> are increased to 0.90 and 1.10, respectively, due to the reducing properties of Ce<sup>3+</sup> as shown in Eq. (7). Besides, the binding energies of Ca2p<sub>1/2</sub> and Ca2p<sub>3/2</sub> as shown in Fig. S2a exhibit a separation of 3.5 eV and an intensity ratio of 1/2, indicating the existing of Ca<sup>2+</sup> [59]. Fig. S2b displays the high resolution spectrum for O1s, which exhibits three different peaks (marked as O1, O2, and O3), corresponding to the metal oxygen bonds (O1, ~529.5 eV), oxygen ions (O2, ~531.2 eV) and physic or chemisorbed water at or within the

surface (O3, ~533.1 eV) [61]. Based on these analyses, the surface of as-prepared DFMs possesses a composition containing Ni<sup>2+</sup>, Ni<sup>3+</sup>, Ca<sup>2+</sup>, and O<sup>2-</sup>.



### 3.2. Integrated $\text{CO}_2$ capture and conversion performance

The integrated  $\text{CO}_2$  capture and conversion performances of DFMs are depicted in Fig. 7. The difference between the recorded  $\text{CO}_2$  concentrations in the outlet gas stream during  $\text{CO}_2$  capture stage and a blank experiment (as shown in Fig. S3, i.e., without any  $\text{CO}_2$  sorbent) is equal to the capacity of  $\text{CO}_2$  captured. The integrated  $\text{CO}_2$  capture and conversion performance, as well as the TOF derived from different DFMs, are summarised in Table 3. The example of TOF calculation is shown in supporting information. The capture capacity of the synthesized CaO is determined as 15.7 mmol g<sup>-1</sup> in the first step, which is much higher than that reported in the previous literature due to the porous structure generated by the sol-gel method [64,65]. In the second step, a flow of 100 ml min<sup>-1</sup> of 5% H<sub>2</sub> balanced with N<sub>2</sub>, ensuring a ratio of H<sub>2</sub> to  $\text{CO}_2$  over 3:1, is used. Only a small amount of CO (3.2 mmol g<sup>-1</sup>) is observed in Fig. S4a for the synthesized CaO due to the absence of Ni active sites, while the majority of captured  $\text{CO}_2$  (7.6 mmol g<sup>-1</sup>) is released through the regeneration of the DFMs in the H<sub>2</sub> atmosphere. The  $\text{CO}_2$  conversion is only 23.4% without the

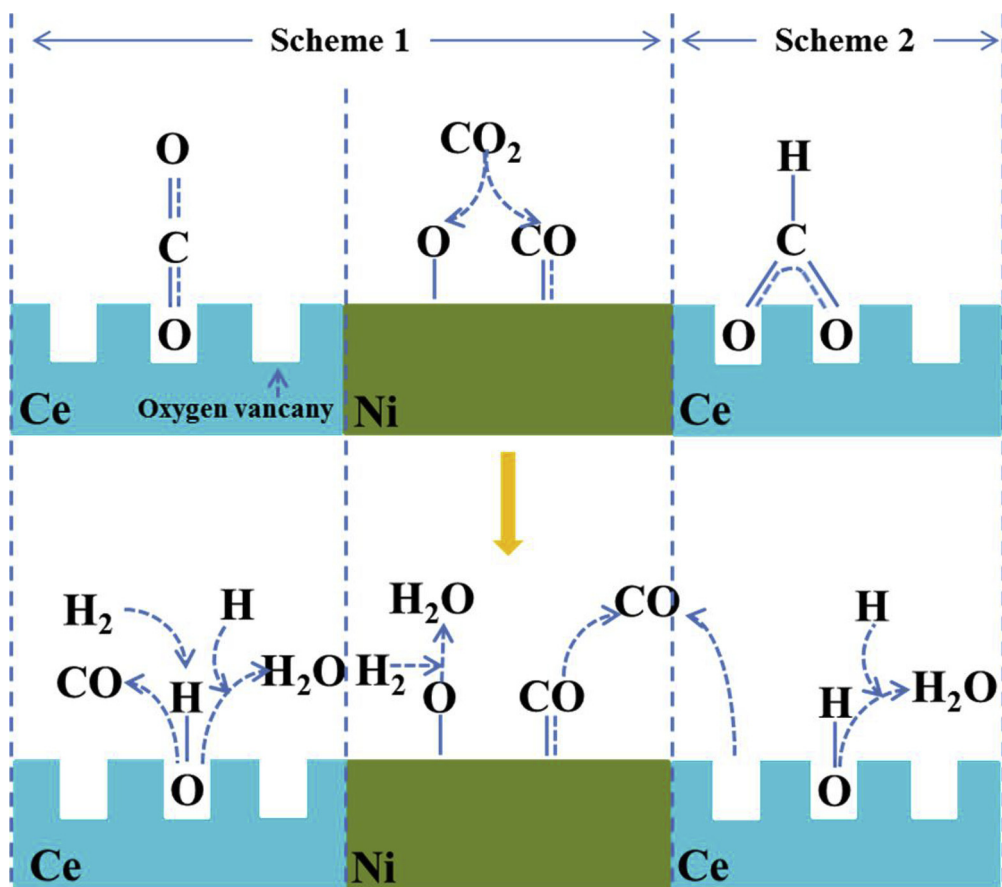
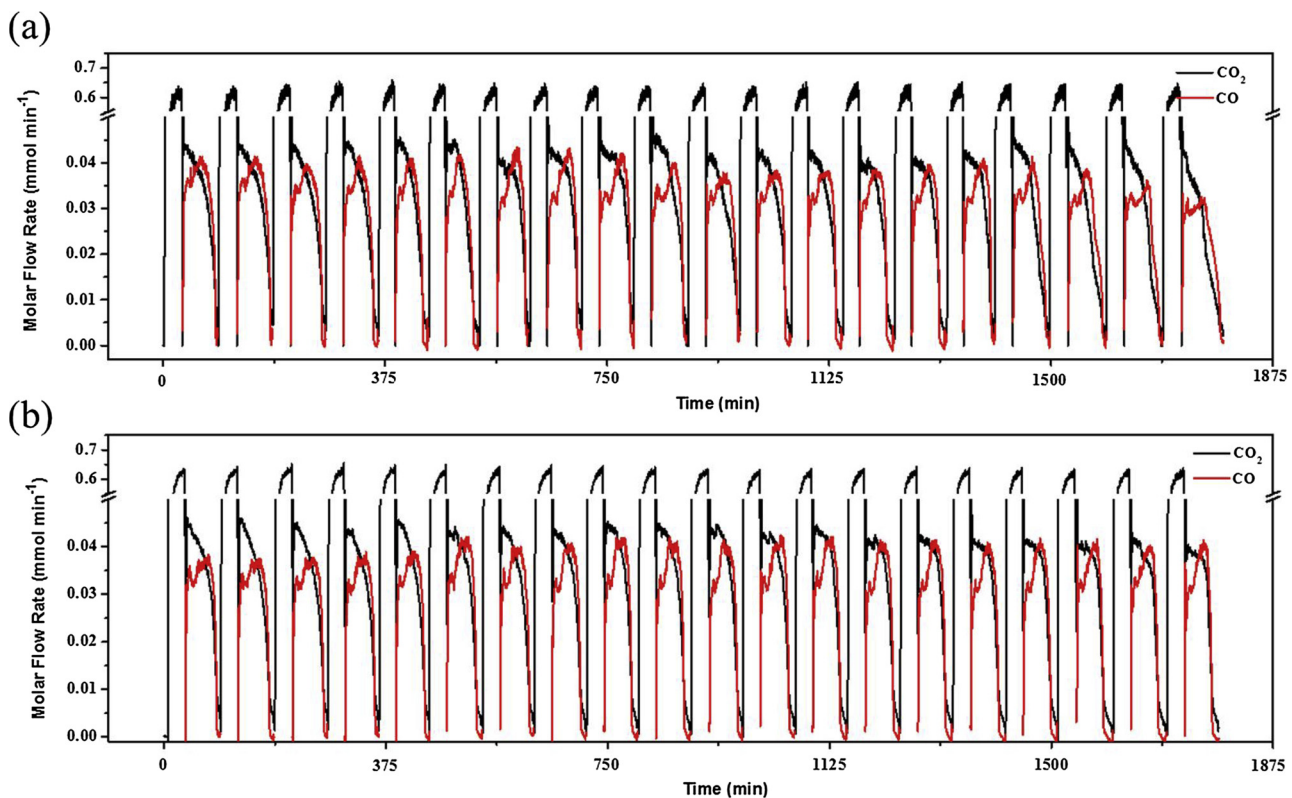


Fig. 9. Reaction mechanism of the RWGS reaction over DFM.

Fig. 10. Cyclic  $\text{CO}_2$  capture and conversion reactions of (a)  $\text{Ca}_1\text{Ni}_{0.1}$ ; (b)  $\text{Ca}_1\text{Ni}_{0.1}\text{Ce}_{0.033}$ .

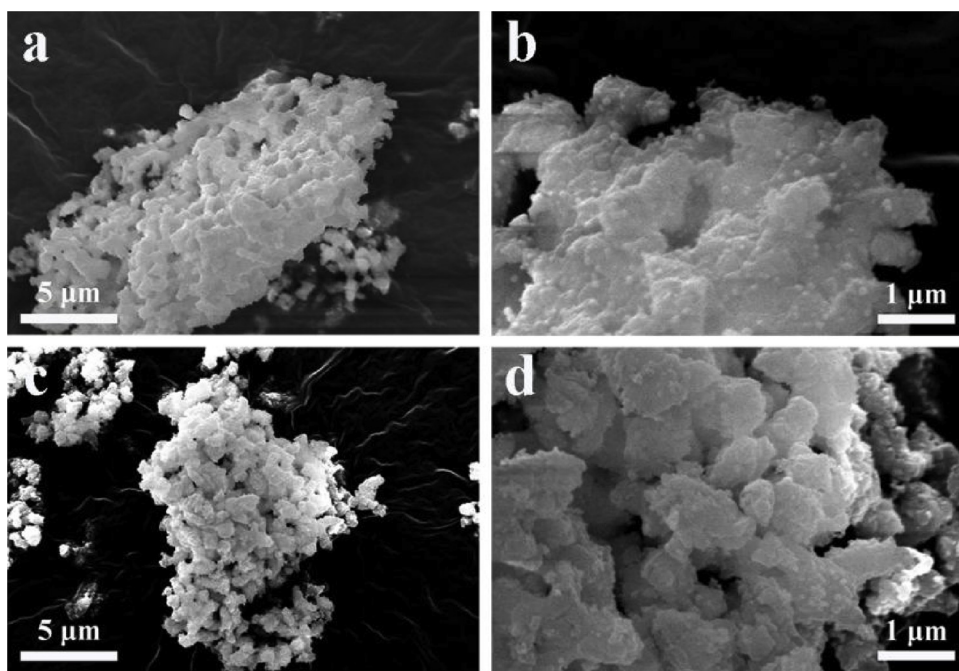


Fig. 11. SEM images of DFM samples after 20 cycles of integrated  $\text{CO}_2$  capture and conversion (a) and (b)  $\text{Ca}_1\text{Ni}_{0.1}$ , (c) and (d)  $\text{Ca}_1\text{Ni}_{0.1}\text{Ce}_{0.033}$ .

introduction of Ni and Ce species. The unreleased  $\text{CO}_2$  is proposed to be contained inside the synthesized  $\text{CaO}$  as the regeneration temperature is the same as capturing temperature.

After the incorporation of Ni,  $\text{CO}_2$  capture capacity is slightly decreased due to the reduced mass content of  $\text{CaO}$  in the DFM samples and CO yield is dramatically increased to  $6.9 \text{ mmol g}^{-1}$  as shown in Fig. 7a indicating that the addition of Ni can promote the reaction of Eq. (3) in a positive direction through the reaction of  $\text{CO}_2$  and  $\text{H}_2$ . After the incorporation of Ce with a Ca/Ce molar ratio of 1:0.017, the CO yield is slightly increased in Fig. S4b because of the small amount doping of Ce. Further increasing the loading of Ce,  $\text{Ca}_1\text{Ni}_{0.1}\text{Ce}_{0.033}$  (Fig. 7b) exhibits the best integrated  $\text{CO}_2$  capture and conversion performance with a highest CO yield ( $7.3 \text{ mmol g}^{-1}$ ) and a relatively lower  $\text{CO}_2$  yield ( $6.7 \text{ mmol g}^{-1}$ ). The highest TOF of the  $\text{Ca}_1\text{Ni}_{0.1}\text{Ce}_{0.033}$  is  $0.78 \text{ s}^{-1}$  indicating a promising catalytic activity of the  $\text{Ca}_1\text{Ni}_{0.1}\text{Ce}_{0.033}$  due to the enhanced oxygen storage capacity of Ca-Ce promoted the catalytic performance of Ni species. The  $\text{Ca}_1\text{Ni}_{0.1}\text{Ce}_{0.033}$  exhibits the highest  $\text{CO}_2$  conversion of 51.8% coupled with a nearly 100% CO selectivity, which is much better than the performance reported by Ranjbar et al. ( $\text{CO}_2$  conversion and CO selectivity are 38% and 95%, respectively at  $650 \text{ }^\circ\text{C}$  with 10% Ni loading) [66] and Wang et al. ( $\text{CO}_2$  conversion and CO selectivity are 38% and 100%, respectively at  $600 \text{ }^\circ\text{C}$  with 10% Co loading) [67]. The detailed comparison of integrated  $\text{CO}_2$  capture and conversion and reported in the literature are summarised in Table S1. It is found that compared to the conventional RWGS reaction, the performance of integrated  $\text{CO}_2$  capture and conversion proposed in this work exhibits a good  $\text{CO}_2$  conversion and a remarkable CO selectivity, as well as a good stability.

To date, two main reaction mechanisms have been proposed: a redox process (Scheme 1) [68–70] and an associative “formate” mechanism (Scheme 2) [71–73].

#### Scheme 1:



#### Scheme 2:



In the redox mechanism, the interaction of  $\text{CO}_2$  over oxygen vacancy results in the oxidation of catalyst and release of CO molecule. The oxidized catalyst is subsequently reduced by  $\text{H}_2$ . In the associative mechanism,  $\sigma$  refers to sites on the oxide support. The main reaction intermediate is a bidentate formate, which decomposes to form CO and terminal hydroxyl groups. As shown in Fig. 8 and S5, the in-situ DRIFTS spectra show peaks around  $1780$  and  $2120 \text{ cm}^{-1}$  corresponding to the carbonyl, which is caused by the stretching mode of CO molecules bound at on-top metal sites. The characteristic peaks around  $2450$ ,  $2850$  and  $2950 \text{ cm}^{-1}$  are assigned to the formate species, indicating the co-existence of Scheme 1 and 2. The spectra of the  $\text{Ca}_1\text{Ni}_{0.1}$  and  $\text{Ca}_1\text{Ni}_{0.1}\text{Ce}_{0.033}$  in Fig. 8 are quite similar to the spectra of  $\text{CaO}$  and  $\text{Ca}_1\text{Ni}_{0.1}\text{Ce}_{0.017}$  in Fig. S5. However, the performance of integrated  $\text{CO}_2$  capture and conversion exhibits a great difference between various DFM samples. Thus, we propose that the surface formate and carbonyl observed by DRIFTS were not the main reaction intermediates to cause the difference between various DFM samples, which has also been reported by Alexandre et al. [74]. Thus, a model for the reaction mechanism of the integrated  $\text{CO}_2$  capture and conversion over DFM samples is proposed in Fig. 9. As for the DFM samples without cerium doping, after switching the gas to  $\text{H}_2$ ,  $\text{CO}_2$  will spillover from the surface of the DFM samples and react with Ni active sites resulting in the formation of CO and  $\text{NiO}$  (Eq. (8)). The reduction of  $\text{NiO}$  by the adsorbed  $\text{H}_2$  species is proposed by Eq. (9). In this case,  $\text{Ni}^{2+}$  becomes Ni and the oxygen reacts with hydrogen to form water.  $\text{Ce}^{3+}$  and  $\text{Ce}^{4+}$  represent reduced ceria (oxygen vacancy) and oxidized ceria, respectively. After the incorporation of cerium, the first step involves the interaction of  $\text{CO}_2$  over oxygen vacancy resulting in the oxidation of catalyst and release of CO molecule as represented by Eq.

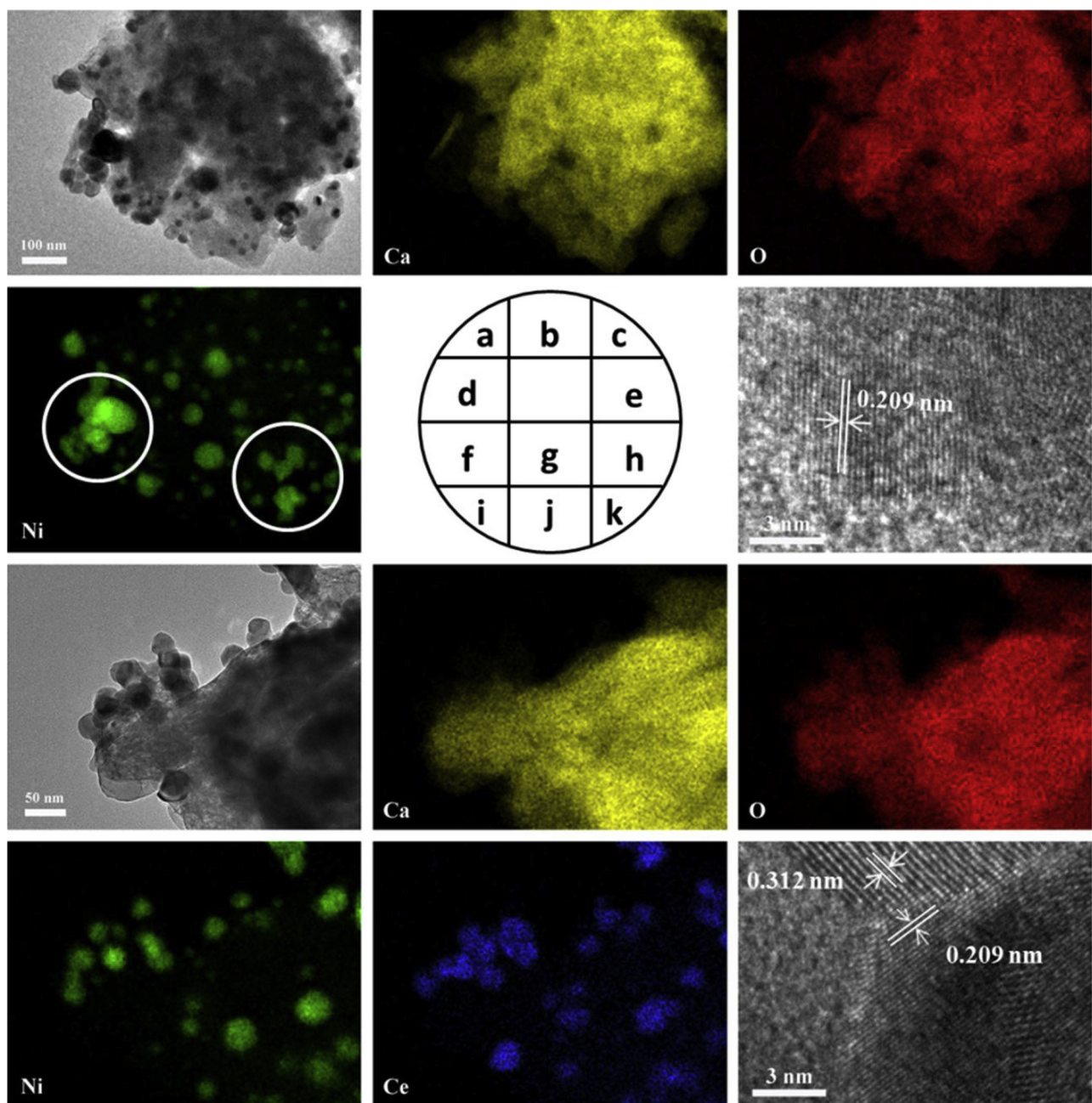


**Fig. 12.** TEM, elemental mappings and high-resolution TEM images of DFMs after 20 cycles of integrated  $\text{CO}_2$  capture and conversion (a–e)  $\text{Ca}_1\text{Ni}_{0.1}$ , (f–k)  $\text{Ca}_1\text{Ni}_{0.1}\text{Ce}_{0.033}$ .

(10). The adsorbed  $\text{H}_2$  species extracts lattice oxygen from ceria, giving out  $\text{H}_2\text{O}$  molecule along with the reduction of catalyst (Eq. (11)).

The influence of reaction temperature was studied using the  $\text{Ca}_1\text{Ni}_{0.1}\text{Ce}_{0.033}$  catalyst. When increasing the carbon capture and conversion temperature from 650 to 700 and further to 750  $^\circ\text{C}$ , as shown in Fig. S6, it is found that the decomposition rate of  $\text{CaCO}_3$  is dramatically increased after switching to  $\text{H}_2$ . However, the rate of the RWGS reaction is marginally increased due to the controlling step of  $\text{CO}_2$  conversion with limited active Ni species. Therefore, 650  $^\circ\text{C}$  is optimal for carbon capture and CO production in this work.

### 3.3. Cyclic $\text{CO}_2$ capture and conversion performance

The cyclic performance of the integrated  $\text{CO}_2$  capture and conversion of DFMs with the doping of Ce is evaluated by 20 cycles and the

experimental results are presented in Fig. 10. The  $\text{Ca}_1\text{Ni}_{0.1}$  shows an initial CO released capacity of 6.9  $\text{mmol g}^{-1}$ ; however, the CO released capacity is reduced rapidly with increasing cycle numbers, dropping to about 4.6  $\text{mmol g}^{-1}$  at the 20th cycle. This decay of carbonation conversion over repeated cycles is attributed to the agglomeration and sintering of unsupported  $\text{CaO}$  and the carbon deposition of the Ni-based catalyst. However, it shows that the integrated  $\text{CO}_2$  capture and conversion performance of  $\text{Ca}_1\text{Ni}_{0.1}\text{Ce}_{0.033}$  is kept completely unchangeable after 20 cycles due to the doping of  $\text{CeO}_2$ . The decay of  $\text{CO}_2$  conversion in the  $\text{Ca}_1\text{Ni}_{0.1}$  is not caused by the deposited carbon on the active sites due to no peak can be observed in the Raman spectra in Fig. S7.

Fig. 11 displays the SEM images of DFMs after 20 cycles of integrated  $\text{CO}_2$  capture and conversion. By comparing the porous structure, the obvious changes can be observed between the spent  $\text{Ca}_1\text{Ni}_{0.1}$

and  $\text{Ca}_1\text{Ni}_{0.1}\text{Ce}_{0.033}$ . As for the  $\text{Ca}_1\text{Ni}_{0.1}$ , the porous structure is almost disappeared and the surface morphology is changed into a bulk structure, indicating the sintering of  $\text{CaO}$  particles and  $\text{Ni}$  active sites, which is in agreement with the performance after 20 cycles of integrated  $\text{CO}_2$  capture and conversion. However, a porous structure is observed for the  $\text{Ca}_1\text{Ni}_{0.1}\text{Ce}_{0.033}$  after 20 cycles of integrated  $\text{CO}_2$  capture and conversion due to the doping of  $\text{CeO}_2$  acting as a support of DFM. This porous structure can also be confirmed by the  $\text{N}_2$  adsorption-desorption isotherms and pore size distribution in Fig. S8. Compared with  $\text{Ca}_1\text{Ni}_{0.1}\text{Ce}_{0.017}$ ,  $\text{Ca}_1\text{Ni}_{0.1}\text{Ce}_{0.033}$  exhibited a higher surface area and pore volume, as well as an obvious distribution of mesopores and macropores ranging from 10 to 100 nm. Thus, the Ce-doped DFM exhibited an excellent stability in the integrated  $\text{CO}_2$  capture and conversion. The XRD results of the spent DFM are shown in Fig. S9. In  $\text{Ca}_1\text{Ni}_{0.1}$ , only low-intensity peaks attributed to  $\text{Ca}(\text{OH})_2$  can be observed. However, the spent  $\text{Ca}_1\text{Ni}_{0.1}\text{Ce}_{0.033}$  exhibited strong peaks assigned to  $\text{Ca}(\text{OH})_2$ . The formation of abundant  $\text{Ca}(\text{OH})_2$  is attributed to the reaction between  $\text{CaO}$  and  $\text{H}_2\text{O}$  produced by the RWGS reaction after the incorporation of  $\text{CeO}_2$ . In addition, after 20 cycles of integrated  $\text{CO}_2$  capture and conversion, all the  $\text{NiO}$  compounds in DFM were converted into monotonic  $\text{Ni}$ , indicating that the nickel oxides can be reduced into metallic  $\text{Ni}$  after the introduction of  $\text{H}_2$  during the integrated  $\text{CO}_2$  capture and conversion without an additional catalyst reduction process.

The porous structure and particles distribution of DFM after 20 cycles of integrated  $\text{CO}_2$  capture and conversion are characterized by TEM and HRTEM, as presented in Fig. 12. It is evident that the porous structure of  $\text{Ca}_1\text{Ni}_{0.1}$  is almost disappeared and the  $\text{Ni}$  element mapping exhibits an agglomeration, which is in agreement with the SEM images. In addition, the metal particle size of  $\text{Ca}_1\text{Ni}_{0.1}$  after 20 integrated cycles is dramatically increased as shown in Fig. S10. The exposed planes are (202) planes of  $\text{NiO}$  with an interplanar spacing of 0.209 nm calculated from the corresponding HRTEM images. After the incorporation of Ce, the  $\text{Ca}_1\text{Ni}_{0.1}\text{Ce}_{0.033}$  still exhibits a porous structure with a uniform distribution of  $\text{Ni}$  element after 20 integrated cycles and the metal particle size is slightly increased due to the  $\text{CeO}_2$  acting as a physical barrier to prevent the aggregation of  $\text{Ni}$  active sites. The interplanar spacing of 0.312 nm and 0.209 nm represent (111) lattice plane of  $\text{CeO}_2$  and (202) lattice plane of  $\text{NiO}$ , respectively.

#### 4. Conclusions

The  $\text{CO}_2$  capture and conversion process integrating the RWGS directly into  $\text{CO}_2$  capture is proposed using a one-pot method synthesized DFM, which contain a sorbent coupled with a catalyst component. In this integrated process, the sorbent regeneration and  $\text{CO}_2$  conversion are performed simultaneously in a single reactor, requiring no additional heat input. The synthetic natural gas can be recycled to an industrial facility, conserving fuel while reducing  $\text{CO}_2$  emissions. It is found that with the incorporation of  $\text{CeO}_2$ , the DFM exhibited an outstanding CO yield ( $7.3 \text{ mmol g}^{-1}$ ) and the highest TOF value ( $0.78 \text{ s}^{-1}$ ) due to the dissociated  $\text{CO}_2$  can be directly oxidized by the oxygen vacancies generated by the ceria support. In addition, the dissociated  $\text{CO}_2$  and hydrogen over nickel surface can directly form CO and supply spillover hydrogen to nearby oxygen vacancies, respectively. After 20 cycles of integrated  $\text{CO}_2$  capture and conversion, the Ce-doping DFM exhibit an excellent stability due to the well-dispersed  $\text{CeO}_2$ , which could act as a physical barrier, effectively prevents the growth and agglomeration of  $\text{CaO}$  crystallite and  $\text{NiO}$  species.

#### Acknowledgements

The authors are grateful for the financial support of National Natural Science Foundation of China (no. 21706050), SOAR Fellowship at the University of Sydney and China Scholarship Council (CSC, no. 201606450016).

#### Appendix A. Supplementary data

Supplementary data associated with this article can be found, in the online version, at <https://doi.org/10.1016/j.apcatb.2018.11.040>.

#### References

- [1] IPCC, Climate Change 2014: Mitigation of Climate Change, Cambridge University Press, 2015.
- [2] E. Haque, M.M. Islam, E. Pourazadi, S. Sarkar, A.T. Harris, A.I. Minett, E. Yamaz, S.M. Alshehri, Y. Ide, K.C.W. Wu, *Chem.-Asian J.* 12 (2017) 283–288.
- [3] C.J. Rhodes, *Sci. Prog.* 99 (2016) 97–104.
- [4] J. Rogelj, M. den Elzen, N. Höhne, T. Fransen, H. Fekete, H. Winkler, R. Schaeffer, F. Sha, K. Riahi, M. Meinshausen, *Nature* 534 (2016) 631.
- [5] B. Mandal, S. Bandyopadhyay, *Chem. Eng. Sci.* 61 (2006) 5440–5447.
- [6] A.L. Chaffee, G.P. Knowles, Z. Liang, J. Zhang, P. Xiao, P.A. Webley, *Int. J. Greenh. Gas Con.* 1 (2007) 11–18.
- [7] C. Zhao, X. Chen, C. Zhao, *Energy Fuels* 24 (2010) 1009–1012.
- [8] Y. Liang, D. Harrison, R. Gupta, D. Green, W. McMichael, *Energy Fuels* 18 (2004) 569–575.
- [9] J. Ren, L.B. Wu, B.G. Li, *Ind. Eng. Chem. Res.* 51 (2012) 7901–7909.
- [10] B.F. Goodrich, J.C. de la Fuente, B.E. Gurkan, Z.K. Lopez, E.A. Price, Y. Huang, J.F. Brennecke, *J. Phys. Chem. B* 115 (2011) 9140–9150.
- [11] Y.T. Liao, S. Dutta, C.H. Chien, C.C. Hu, F.K. Shieh, C.H. Lin, K.C.W. Wu, *J. Inorg. Organomet. Polym.* 25 (2015) 251–258.
- [12] S. Lee, T.P. Filburn, M. Gray, J.W. Park, H.J. Song, *Ind. Eng. Chem. Res.* 47 (2008) 7419–7423.
- [13] J. Blamey, E. Anthony, J. Wang, P. Fennell, *Prog. Energy Combust. Sci.* 36 (2010) 260–279.
- [14] M. Erans, V. Manovic, E.J. Anthony, *Appl. Energy* 180 (2016) 722–742.
- [15] A. Perejón, L.M. Romeo, Y. Lara, P. Lisboa, A. Martínez, J.M. Valverde, *Appl. Energy* 162 (2016) 787–807.
- [16] T. Shimizu, T. Hirama, H. Hosoda, K. Kitano, M. Inagaki, K. Tejima, *Chem. Eng. Res. Des.* 77 (1999) 62–68.
- [17] W. Liu, H. An, C. Qin, J. Yin, G. Wang, B. Feng, M. Xu, *Energy Fuels* 26 (2012) 2751–2767.
- [18] J.M. Valverde, *J. Mater. Chem. A* 1 (2013) 447–468.
- [19] M. Alonso, Y. Criado, J. Abanades, G. Grasa, *Fuel* 127 (2014) 52–61.
- [20] J.C. Abanades, G. Grasa, M. Alonso, N. Rodriguez, E.J. Anthony, L.M. Romeo, *Environ. Sci. Technol.* 41 (2007) 5523–5527.
- [21] A. Mackenzie, D. Granatstein, E.J. Anthony, J. Abanades, *Energy Fuels* 21 (2007) 920–926.
- [22] J. Miranda-Pizarro, A. Perejón, J.M. Valverde, L.A. Pérez-Maqueda, P.E. Sánchez-Jiménez, *Fuel* 196 (2017) 497–507.
- [23] X. Ma, Y. Li, C. Chi, W. Zhang, J. Shi, L. Duan, *Energy Fuel* 31 (2017) 7299–7308.
- [24] M. Erans, M. Jeremias, L. Zheng, J.G. Yao, J. Blamey, V. Manovic, P.S. Fennell, E.J. Anthony, *Appl. Energy* 225 (2018) 392–401.
- [25] M.S. Duyar, M.A.A. Trevino, R.J. Farrauto, *Appl. Catal. B: Environ.* 168 (2015) 370–376.
- [26] J.C. Abanades, E.S. Rubin, M. Mazzotti, H.J. Herzog, *Energy Environ. Sci.* 10 (2017) 2491–2499.
- [27] R.M. Cuellar Franca, A. Azapagic, *J. CO<sub>2</sub> Util.* 9 (2015) 82–102.
- [28] M. Cai, J. Wen, W. Chu, X. Cheng, Z. Li, *J. Nat. Gas. Chem.* 20 (2011) 318–324.
- [29] M.S. Duyar, S. Wang, M.A. Arellano Trevino, R.J. Farrauto, *J. CO<sub>2</sub> Util.* 15 (2016) 65–71.
- [30] Q. Zheng, R. Farrauto, A. Chau Nguyen, *Ind. Eng. Chem. Res.* 55 (2016) 6768–6776.
- [31] S.M. Kim, P.M. Abdala, M. Broda, D. Hosseini, C. Copéret, C. Müller, *ACS Catal.* 8 (2018) 2815–2823.
- [32] X. Peng, K. Cheng, J. Kang, B. Gu, X. Yu, Q. Zhang, Y. Wang, *Angew. Chem. Int. Ed.* 54 (2015) 4553–4556.
- [33] G. Melaet, W.T. Ralston, C.S. Li, S. Alayoglu, K. An, N. Musselwhite, B. Kalkan, G.A. Somorjai, *J. Am. Chem. Soc.* 136 (2014) 2260–2263.
- [34] Y.A. Daza, R.A. Kent, M.M. Yung, J.N. Kuhn, *Ind. Eng. Chem. Res.* 53 (2014) 5828–5837.
- [35] R.V. Gonçalves, L.L.R. Vono, R. Wojcieszak, C.S.B. Dias, H. Wender, E. Teixeira Neto, L.M. Rossi, *Appl. Catal. B: Environ.* 209 (2017) 240–246.
- [36] A. Brennführer, H. Neumann, M. Beller, *Angew. Chem. Int. Ed.* 48 (2009) 4114–4133.
- [37] X.F. Wu, H. Neumann, M. Beller, *Chem. Soc. Rev.* 40 (2011) 4986–5009.
- [38] H. Sun, C.M. Parlett, M.A. Isaacs, X. Liu, G. Adwek, J. Wang, B. Shen, J. Huang, C. Wu, *Fuel* 235 (2019) 1070–1076.
- [39] S. Wang, S. Fan, L. Fan, Y. Zhao, X. Ma, *Environ. Sci. Technol.* 49 (2015) 5021–5027.
- [40] M. Shokrollahi Yancheshmeh, H.R. Radfarnia, M.C. Iliuta, *ACS Sustain. Chem. Eng.* 5 (2017) 9774–9786.
- [41] F. Sadi, D. Duprez, F. Gérard, A. Miloudi, *J. Catal.* 213 (2003) 226–234.
- [42] A.B. Kehoe, D.O. Scanlon, G.W. Watson, *Chem. Mater.* 23 (2011) 4464–4468.
- [43] X. Du, D. Zhang, L. Shi, R. Gao, J. Zhang, *J. Phys. Chem. C* 116 (2012) 10009–10016.
- [44] A. Kambolis, H. Matralis, A. Tovarelli, C. Papadopoulou, *Appl. Catal. A Gen.* 377 (2010) 16–26.
- [45] V.M. Gonzalez-Delacruz, F. Ternero, R. Perenézquez, A. Caballero, J.P. Holgado, *Appl. Catal. A Gen.* 384 (2010) 1–9.
- [46] H. Sun, C. Wu, B. Shen, X. Zhang, Y. Zhang, J. Huang, *Mater. Today Sustain.* (2018).

[47] E. Santos, C. Alfonsín, A. Chambel, A. Fernandes, A.S. Dias, C. Pinheiro, M. Ribeiro, *Fuel* 94 (2012) 624–628.

[48] F. Jin, H. Sun, C. Wu, H. Ling, Y. Jiang, P.T. Williams, J. Huang, *Catal. Today* 309 (2018) 2–10.

[49] H. Roh, I. Eum, D. Jeong, *Renew. Energy* 42 (2012) 212–216.

[50] D. Yao, Y. Zhang, P.T. Williams, H. Yang, H. Chen, *Appl. Catal. B: Environ.* 221 (2018) 584–597.

[51] M. Zhang, Y. Peng, Y. Sun, P. Li, J. Yu, *Fuel* 111 (2013) 636–642.

[52] H. Guo, X. Kou, Y. Zhao, S. Wang, Q. Sun, X. Ma, *Chem. Eng. J.* 334 (2018) 237–246.

[53] D. Alvarez, J.C. Abanades, *Ind. Eng. Chem. Res.* 44 (2005) 5608–5615.

[54] L. Katta, P. Sudarsanam, G. Thrimurthulu, B.M. Reddy, *Appl. Catal. B: Environ.* 101 (2010) 101–108.

[55] X. Wen, C. Li, X. Fan, H. Gao, W. Zhang, L. Chen, G. Zeng, Y. Zhao, *Energy Fuels* 25 (2011) 2939–2944.

[56] H. Guo, J. Feng, Y. Zhao, S. Wang, X. Ma, *J. CO<sub>2</sub> Util.* 19 (2017) 165–176.

[57] H. Lu, A. Khan, S.E. Pratsinis, P.G. Smirniotis, *Energy Fuels* 23 (2008) 1093–1100.

[58] A. Antzara, E. Heracleous, A.A. Lemonidou, *Appl. Energy* 156 (2015) 331–343.

[59] M.L. Granados, A. Gurbani, R. Mariscal, J. Fierro, *J. Catal.* 256 (2008) 172–182.

[60] Z. Fang, B. Yuan, T. Lin, H. Xu, Y. Cao, Z. Shi, M. Gong, Y. Chen, *Chem. Eng. Res. Des.* 94 (2015) 648–659.

[61] D. Li, Y. Gong, Y. Zhang, C. Luo, W. Li, Q. Fu, C. Pan, *Sci. Rep.* 5 (2015) 12903.

[62] L. Liu, H. Zhang, J. Yang, Y. Mu, Y. Wang, *J. Mater. Chem. A* 3 (2015) 22393–22403.

[63] J. Xiao, S. Yang, *J. Mater. Chem.* 22 (2012) 12253–12262.

[64] M. Broda, A.M. Kierzkowska, C.R. Müller, *Environ. Sci. Technol.* 46 (2012) 10849–10856.

[65] S. Wu, Y. Zhu, *Ind. Eng. Chem. Res.* 49 (2010) 2701–2706.

[66] A. Ranjbar, A. Irankhah, S.F. Aghamiri, *J. Environ. Chem. Eng.* 6 (2018) 4945–4952.

[67] L. Wang, H. Liu, Y. Chen, S. Yang, *Int. J. Hydrogen Energy* 42 (2017) 3682–3689.

[68] S. Hilaire, X. Wang, T. Luo, R. Gorte, J. Wagner, *Appl. Catal. A Gen.* 215 (2001) 271–278.

[69] R. Gorte, S. Zhao, *Catal. Today* 104 (2005) 18–24.

[70] Y. Liu, Z. Li, H. Xu, Y. Han, *Catal. Commun.* 76 (2016) 1–6.

[71] G. Jacobs, L. Williams, U. Graham, D. Sparks, B.H. Davis, *J. Phys. Chem. B* 107 (2003) 10398–10404.

[72] G. Jacobs, E. Chenu, P.M. Patterson, L. Williams, D. Sparks, G. Thomas, B.H. Davis, *Appl. Catal. A Gen.* 258 (2004) 203–214.

[73] G. Jacobs, U.M. Graham, E. Chenu, P.M. Patterson, A. Dozier, B.H. Davis, *J. Catal.* 229 (2005) 499–512.

[74] A. Goguet, F.C. Meunier, D. Tibiletti, J.P. Breen, R. Burch, *J. Phys. Chem. B* 108 (2004) 20240–20246.